ELSEVIER

International Journal of Mass Spectrometry 203 (2000) 1–18

International Journal of Mass Spectrometry

Review

Binding energy of van der Waals- and hydrogen-bonded clusters by threshold ionization techniques

J.E. Braun, Th. Mehnert, H.J. Neusser*

Institut für Physikalische und Theoretische Chemie, Technische Universität München, Lichtenbergstrasse 4, D-85748 Garching, Germany

Received 10 July 2000; accepted 23 September 2000

Abstract

Mass analyzed threshold ionization is based on the laser excitation of high long-lived Rydberg states 5–15 cm^{-1} below a selected ionization threshold. Separating the Rydberg molecules from promptly produced ions in a delayed pulsed field ionization scheme leads to state and energy selected ions that are mass analyzed in a time-of-flight mass spectrometer. We present vibrational ion spectra of various clusters of indole, phenol and 1-naphthol. Because of the mass selectivity dissociation thresholds of the clusters can be measured when the ion internal energy is increased and a breakdown of the parent ion signal caused by dissociation is observed. We compare results for van der Waals with hydrogen bond energies and find a strong increase for the latter in the ionized cluster. Experimental results are explained by changes of the electron density distribution in the molecules after clustering and ionization. The influence of the size of the aromatic part of a molecule on the strength of the hydrogen bonding to an attached water molecule is investigated for the neutral as well as for the ionized molecules. In ionic clusters, we observe a decrease of hydrogen bond strength with an increasing number of aromatic rings in the chromophor, whereas the neutral binding energy increases in this case. (Int J Mass Spectrom 203 (2000) 1–18) © 2000 Elsevier Science B.V.

Keywords: Mass analyzed threshold ionization (MATI); Binding energies; Hydrogen bonding; van der Waals cluster; Intermolecular forces

1. Introduction

"Weak" intermolecular forces like the van der Waals or the hydrogen bond play a significant role in a great variety of physical, chemical, and biological phenomena. The effects of these forces manifest themselves, e.g. in the behaviour of real gases, in the special properties of water, or in the process of protein folding. Consequently, a large number of experimental and theoretical studies has been carried out in order to increase our knowledge about the nature of the intermolecular forces (see, e.g. Ref. [1], and references cited therein). In recent years experimental investigations have been shifting from the bulk to isolated clusters with specific intermolecular bonding. Yet, up to now only limited experimental information on structures and binding energies, especially of weakly bound complexes of biologically relevant, medium-sized organic molecules, has been available.

* Corresponding author. E-mail: neusser@ch.tum.de

PII S1387-3806(00)00384-5

In order to obtain such information it is advantageous to analyze isolated complexes in the gas phase, thus excluding perturbing influences of embedding carrier substances such as solvents or crystal lattices. Isolated complexes can be produced in a supersonic jet expansion into the vacuum [2]. In an adiabatic expansion the molecules are normally cooled down to very low temperatures and clusters of different sizes are produced. After the expansion process, the clusters drift collision-free and can be selectively excited and ionized by laser radiation, and finally separated in a mass spectrometer. Investigating ions rather than neutral particles has several advantages. Their trajectories can be easily manipulated by electromagnetic fields and detection of ions is much more feasible than of neutral particles. In addition using thermochemical cycles it is possible to find the binding energy of the neutral species by investigating ionic clusters.

In many cases it is desirable to examine a pure ensemble of ions excited to the same vibrational state with a defined energy because some effects are obscured and not observable at all in a mixed ensemble of ions with a broad distribution of internal energies. The latter normally happens even if photons of a well-defined energy are used for ionization, as the emitted electrons carry away a variable amount of energy spanning the complete range from zero to the maximum energy above the adiabatic ionization energy. Just at the lowest ionization threshold a situation exists with no excess energy left for kinetic energy of the emitted electrons and exclusively “threshold ions” with no internal energy are produced. For higher photon energies exceeding the lowest ionization energy mainly ions with lower energy contents and only few threshold ions are produced. In the ideal case, this gives rise to a steplike behaviour of the total ion current when the frequency of the ionizing laser is tuned to higher energies, each step indicating a new cationic vibrational energy level (for an example, see the upper trace of Fig. 11 in Sec. 4.2.2). However, often these steps are smeared out, particularly for larger molecules with many internal degrees of freedom.

A pure ensemble of energy-selected ions can be obtained by discriminating nonenergy selected background ions from threshold ions. One suitable technique is the photoion photoelectron coincidence (PIPECO) technique, which has been successfully applied to investigate the decay of molecular ions [3,4]: Ions are monitored only when they are detected together with electrons of nearly zero kinetic energy. The sensitivity of this method is restricted since less than one ion–electron pair should be produced and detected per laser pulse. This is particularly a problem when the repetition rate of the laser system or the pulsed valve is limited. Further, the spectral resolution is limited by the resolution of the photoelectron spectrometer.

A novel method suitable for internal energy selected cluster ion production is the technique of mass analyzed threshold ionization (MATI), which is based on the existence of long-lived Rydberg states in the vicinity of different ionization energies [5,6], as described in the following in more detail. With this technique, exclusively threshold ions are detected, which can be investigated in an ion trap [7] or in a time-of-flight (TOF) mass spectrometer [8]. This makes it possible to observe the time evolution of the excited ions, e.g. mass changes due to fragmentation processes as a function of their internal energy. In recent work we have demonstrated that the dissociation of excited van der Waals- or hydrogen-bonded cluster ions can be monitored with the MATI technique by a simultaneous observation of threshold ions in the cluster ion mass channel and the fragment ion mass channel [6]. This allowed us to determine accurate values for the ionic and neutral binding energies of a series of van der Waals-bound or hydrogen-bonded clusters (see, e.g. [6,9–13]. Recently the MATI technique has been also applied by other groups for the determination of adiabatic ionization energies and cationic vibrational states: Knee and co-workers investigated fluorene · Ar_n [14], Brutschy and co-worker fluoro- and chlorobenzene · Ar_n [15,16], Gerhards et al. dihydroxybenzenes [17], and Müller-Dethlefs and co-workers the phenol · CO cluster [18]. In this work we would like to review the outcome of recent research and present additional new results on hydrogen-bonded clusters like indole · water, indole · benzene, phenol · water, and 1-naph-

thol · water. Further, we will compare the experimental results with ab initio calculations, and discuss the similarities and differences of several types of hydrogen bonds like the N–H · · · O or the O–H · · · O bonds.

2. Experimental methods

2.1. Breakdown measurements

A feasible technique to study the energetics of molecular compounds is the method of "breakdown graphs." Here the total ion current at distinct masses is measured as a function of the energy of the ionizing photon, and all kinds of ions are detected. With this method a great variety of data on the dissociation energy of neutral and ionic dimers and larger clusters has been obtained [8,19–22]. The accuracy of this technique is limited mainly by the width of the internal energy distribution of the ions. In our group it was used for cluster ions of homogeneous constituents with a strong charge resonance interaction leading to binding energies between 0.5 and 1 eV [20].

The energetics of a dissociation reaction of a heterodimer consisting of two molecules A and B can be described by simple relations (see Fig. 1 for illustration):

$$D_0 = \mathrm{AE} - \mathrm{IE(A)} \quad (1)$$

$$E_0 = \mathrm{AE} - \mathrm{IE(A \cdot B)} \quad (2)$$

with D_0 the binding energy (BE) of the neutral dimer A · B and E_0 the BE of the charged cluster A^+ · B. IE(A) and IE(A · B) are the ionization energies of the monomer A and the (hetero)dimer A · B, respectively, and AE is the appearance energy for the dissociation of the dimer cation A^+ · B into A^+ and B. As shown in Fig. 1, by measuring AE, IE(A) and IE(A · B), the binding energies D_0 (neutral) and E_0 (cationic) can be determined. Though the breakdown method is broadly applicable, it suffers from several disadvantages. (1) Especially for clusters, the ionization energy often cannot be determined unambiguously since the Franck-Condon factors for transitions to the vibrationless cationic ground state are often very weak. (2) Sometimes it is difficult to distinguish between monomer ions that have been produced by direct ionization of a neutral monomer and monomer ions originating from the dissociation of the cluster ion. (3) The dissociation threshold is not well determined since a defined photon energy does not lead to a defined internal energy and no sharp dissociation threshold can be found.

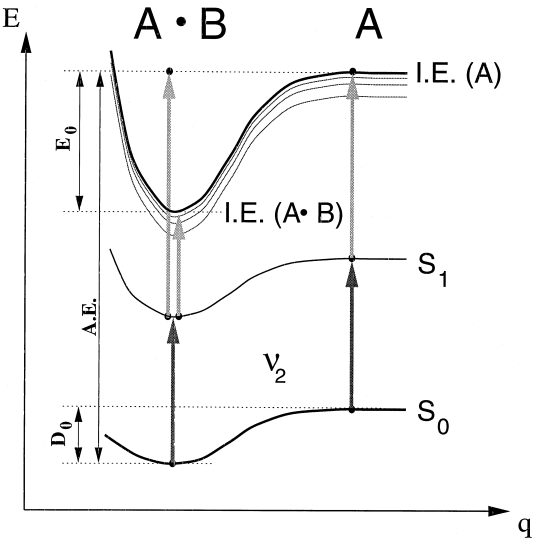

Fig. 1. Potential curves of a cluster A · B. q is the generalized intermolecular distance. D_0 and E_0 are the binding energies for the neutral ground state and the cationic ground state, IE(A), IE(B) the adiabatic ionization energies, and A.E. the appearance energy for ionic cluster fragments. The arrows indicate the resonance-enhanced two-photon ionization process in the cluster and the molecule A.

2.2. Threshold ionization spectroscopy

Threshold ionization methods are based on the existence of extraordinarily long-lived Rydberg states with high principal quantum numbers n and large angular momentum quantum numbers $l \approx n$. These hydrogen atomlike electronic states are populated after excitation to an energy closely below an ionization threshold of the investigated system and can be excited in atoms [23–25], polyatomic molecules [26,27], and even in clusters [28]. As an explanation for the long lifetimes, coupling processes like (l, m_l)

mixing induced by weak electric stray fields or by the dipole interaction of the ionic core during the excitation have been discussed [29–34]. Recent high resolution optical double resonance experiments of our group resolving high Rydberg states ($40 \lesssim n \lesssim 110$) [27] confirm that the lifetime in the microsecond range is indeed longer than that extrapolated from lifetimes of low Rydberg states using the n^3 scaling law [35,36].

There exist several Rydberg series, each series converging to a respective rovibrational eigenstate of the molecular or cluster cation. Deviations from the $1/r$ coulomb potential and higher order (multipole) couplings of the positively charged core to the Rydberg electron are practically negligible for long-lived Rydberg states with high n and l quantum numbers (the high Rydberg electron considers the ionic core as a pointlike charge). Therefore, high Rydberg states located close to the respective ionization energy and their series limits denote the energetic position of the rovibrational eigenstates of the ionic core with high precision.

In order to monitor molecules or clusters excited to high Rydberg states, the weakly bound Rydberg electrons have to be detached from the ionic cores by applying a pulsed electric field. After this, either the released electrons or the threshold ions are detected and monitored as a function of the ionizing laser wavelength. First, the technique of pulsed-field ionization (PFI) has been used to detect the "zero kinetic energy" electrons in high Rydberg states (ZEKE-PFI spectroscopy [37]). An electric ionization field is applied about 1 μs after laser excitation, in a way that promptly produced electrons from fast ionization processes have already been drawn out of the detection region by ubiquitous weak electric stray fields. The stronger the ionization field, the broader are the resulting peaks, because lower n Rydberg states are ionized that are farer away from the ionization energy, according to $\Delta E\ (\mathrm{cm}^{-1}) = \alpha\sqrt{E\ (\mathrm{V/cm})}$ with a value for α varying from 3.2 to 6.1 [23,38]. The ZEKE-PFI technique has displayed a considerably increased resolution in photoelectron spectroscopy of the electronic ground state ions and was successfully applied to a variety of molecules and van der Waals complexes ([39–41], and references therein).

Later, Zhu and Johnson developed a method to combine pulsed field ionization with ion instead of electron detection leading to mass analyzed threshold ionization (MATI) spectroscopy [5]. They separated the threshold ions from promptly produced ions that are responsible for the broad background in photoionization efficiency spectra by a special configuration of electric fields. The spectral resolution and sensitivity of MATI is somewhat lower than that of ZEKE because (1) a relatively strong electric field of about 1 V/cm for the separation of the threshold ions from background ions is required, destroying the highest Rydberg states that contribute to most of the signal in ZEKE experiments, (2) separation times of about 10 μs and more have to be used in which many Rydberg states decay, and (3) a strong electric field of about 1000 V/cm is used for the field ionization and subsequent acceleration of threshold ions affecting relatively low lying Rydberg states and causing a broadening of the peaks. On the other hand, the clear advantage of the MATI technique is its mass selectivity, which is essential for cluster dissociation experiments presented in this work. (For the purpose of this work a high spectral resolution is not necessary.) Recently, we demonstrated that the limited resolution of ZEKE and MATI spectroscopies can be improved by a Rydberg series extrapolation technique after selective detection of high Rydberg series using high resolution lasers [42].

The principle excitation scheme of pulsed field threshold ionization combined with resonance-enhanced two-photon excitation is illustrated in Fig. 2. The wavelength of the first laser with photon energy $h\nu_1$ is tuned to a vibrational band in the $S_1 \leftarrow S_0$ transition of the investigated system. The second laser frequency ν_2 is scanned across the adiabatic ionization energy (AIE) and ionic vibrational states above the AIE. Recording the total ion current leads to a photoionization efficiency curve with steps at the individual lowest thresholds (see left-hand side of Fig. 2 and Fig. 12 in Sec. 4.2.2). In addition to the prompt ionization, molecules in long-lived high (n, l) Rydberg states are excited, surviving the separation pro-

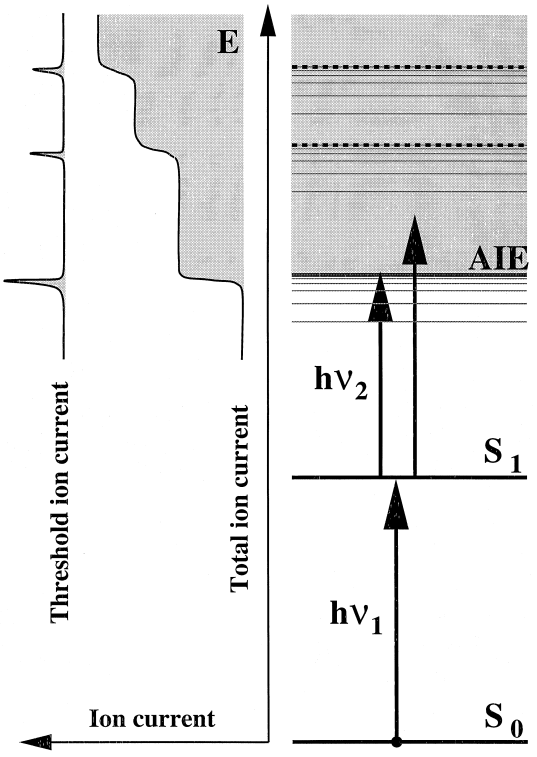

Fig. 2. (Right) Excitation scheme of high Rydberg states in a resonance-enhanced two-photon process. The first photon energy $h\nu_1$ is fixed to a $S_1 \leftarrow S_0$ vibronic transition. The second photon frequency ν_2 frequency is scanned across the lowest ionization energy (AIE) and higher ionization thresholds. (Left) Each ionization threshold leads to a step in the total ion current spectrum and a peak in the threshold ion spectrum.

cess. They are ionized by the delayed pulsed field and the ions are detected exclusively after the MATI separation process as described in the following in detail. As a result, sharp peaks with no background are observed at the individual thresholds. This leads to the vibrational spectrum of the ions as shown schematically on the vertical scale on the left-side of Fig. 2. However, one has to take into account that the ionization threshold is lowered by the weak separation field which causes a shift of the individual thresholds (i.e. of the peaks in the ion spectrum) towards lower energies but does not affect their relative energy distance, yielding the vibrational frequencies we are interested in.

2.2.1. Measuring binding energies

The determination of binding energies (BEs) has been of continuous interest as BE values are important microscopic parameters for the description of the properties of condensed matter. High pressure mass spectrometry [43], IR absorption spectroscopy in gas mixtures [44], or bolometric methods [45] are successful techniques but have not yet been applied to isolated, weakly bound clusters containing larger polyatomic molecules.

The dissociation of weakly bound cluster ions can be observed with the MATI technique as a function of their selected internal energy by the simultaneous observation of threshold ions in the parent and the fragment ion mass channel [6,10]. As a result, we found a signal only at one mass channel at the same time. When the excitation energy is tuned across the appearance energy (see Fig. 1), the signal is "switching" from the dimer ("parent") mass channel to the fragment ("daughter") mass channel in the threshold ion spectrum. The dimer cation cores dissociate into monomer cationic cores and neutral solvent molecules without destroying most of the high Rydberg states [6]. We would like to point out that it is necessary for this method to work that a sufficient number of high Rydberg states survive the cluster dissociation process, as first detected and reported by Krause and Neusser [6,46]. Further, this means that the dissociation rate even at threshold is much faster than the typical time scales of the MATI technique [6]. A prerequisite for the unambiguous determination of the binding energy is that there exist ionic states closely below and above the field free dissociation threshold [47]. This is the case for clusters of large molecules examined in this work.

2.2.2. Field induced Rydberg–core coupling

Recently, we demonstrated for the case of fluorobenzene · Ar clusters that the measured value of the fragment ion appearance energy depends on the strength of the applied ionization field [47]. Signal begins to appear in the fragment mass channel for an energy deposited in the cluster ion core which is several 10 cm^{-1} below the field-free dissociation threshold. The reason for this is a coupling of the

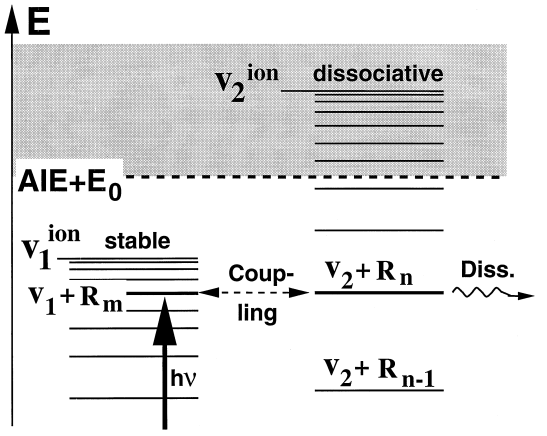

Fig. 3. Coupling of Rydberg states that are members of two different Rydberg series R_m and R_n converging to two different vibrational states v_1, v_2 in the cation. Excitation of high Rydberg states converging to a core vibrational level v_1 below the dissociation threshold. Field-induced Rydberg coupling leads to a transfer of electronic energy to core vibrational energy and finally to a dissociation of the core. For explanation, see text.

originally excited high Rydberg levels of series converging to a vibrational state below the field-free dissociation threshold to lower Rydberg states converging to a vibrational state above the dissociation threshold of the ionic core. The coupling is induced by the pulsed electrical ionization field. The process is illustrated in Fig. 3. The coupling results in a transfer of electronic energy from the excited high Rydberg electron to the vibrational degrees of freedom of the cluster ion core, causing a dissociation of the cluster, even when the total energy is less than AIE + E_0. Here it is assumed that the Rydberg states survive the dissociation, as shown in our recent work [10]. The dissociation can be detected if the ionizing field strength is sufficient to ionize the low Rydberg states of the fragment Rydberg molecule. MATI spectra that are simultaneously recorded at the cluster and the fragment mass channel show an overlap region of $\approx$50 cm^{-1} for the fields used in our experiments. In this internal energy range some clusters dissociate whereas others remain stable, since through the coupling not all clusters gain vibrational energy sufficient for dissociation. This leads to a broadening of the appearance energy range for the daughter ions as was described in detail in our recent work [47]. The coupling has to be taken into account when dissociation thresholds are determined in the MATI experiments (see Sec. 4).

2.2.3. MATI peak shape

As described previously, threshold ions are produced by pulsed-field ionization of high Rydberg states from Rydberg series converging to defined ionization thresholds, i.e. rovibrational states of the cation. For the typical frequency width of the laser pulses (0.1–0.5 cm^{-1}) many rotational intermediate states are populated at the same time. After absorption of the second photon, bunches of Rydberg series are excited and superimposed for the frequency width of the dye lasers and as a consequence the Rydberg structure is not resolved in the relevant high n range. Using Fourier transform-limited laser pulses with a narrow frequency width of 70 MHz both for the population of single rotational states in the S_1 state and excitation of the molecule to high Rydberg states in the second step, the Rydberg series structure can be resolved for $n \lesssim 100$ [28,48,49]. This is demonstrated for the benzene molecule in Fig. 4. In the top part of Fig. 4 the MATI spectrum of benzene with several threshold ion peaks indicating the vibrational states of the cation is displayed. In the bottom part, we demonstrate that for the case of the 6^1 ($\pm$3/2) state of the benzene cation located about 350 cm^{-1} above the AIE, a resolved single Rydberg spectrum from $n \approx 50$ to $n \approx 110$ is measured with high resolution laser pulses and a MATI separation technique [28]. The envelope of the Rydberg series represents the typical structure of the MATI peak with a relatively slow rise and a steep decrease to higher energies. This shape originates from low n ($n \approx 50$) with a small density of states up to closely spaced high n ($n \approx 100$) which are strongly affected by electric fields.

3. Experimental setup

Briefly, the setup for the MATI experiments consists of two dye lasers yielding $\approx$10 ns light pulses with a bandwidth of $\approx$0.3 cm^{-1} (FL 3002, and LPD 3000; Lambda Physik), which are used for the exci-

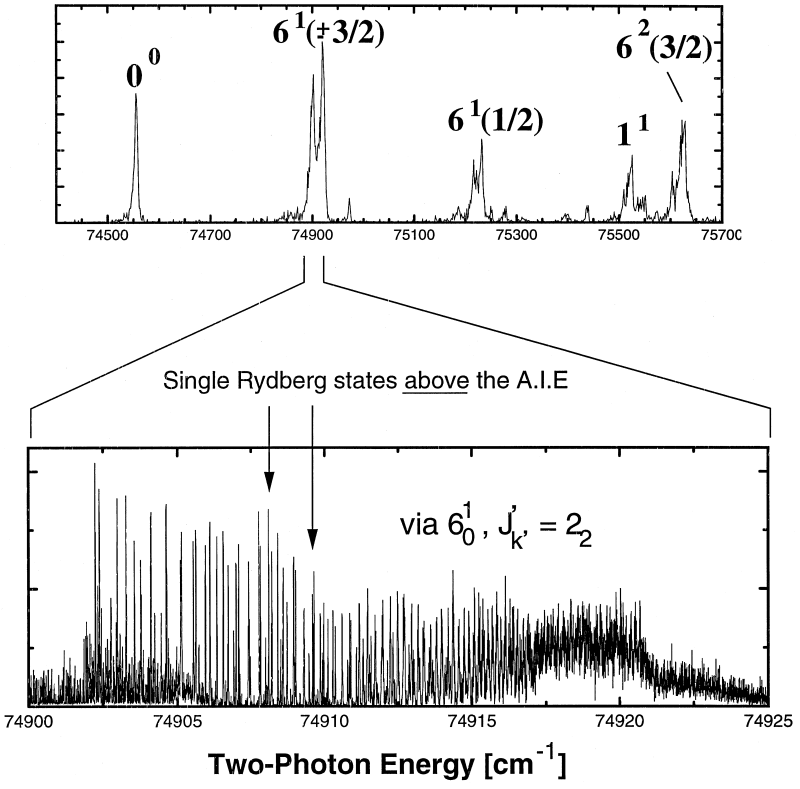

Fig. 4. (Upper part) Threshold ion spectrum of benzene. Each peak results from a unresolved superposition of bunches of high Rydberg states and corresponds to a vibrational level of the benzene cation. (Lower part) Resolved high Rydberg states converging to the 6^1 ($\pm 3/2$) state of the benzene cation measured with a special high resolution laser system. The envelope of the Rydberg series represents the typical structure of the MATI peak. For details, see text.

tation of molecules to high Rydberg levels (MATI) or for the production of ions in a resonantly enhanced two-color two-photon process [resonantly enhanced multiphoton ionization (REMPI)]. Both dye lasers are pumped synchronously by a XeCl excimer laser (EMG 1003i, Lambda Physik). The two counter propagating laser beams intersect a skimmed supersonic molecular beam perpendicularly 15 cm downstream the nozzle orifice. The cold molecular beam is obtained by expanding a gas mixture supersonically into the vacuum. The gas mixture is produced inside a homemade, heatable pulsed (maximum 25 Hz) expansion valve, in which the carrier gas passes the heated sample. The light pulses overlap in time and space in the center of the first stage of a double stage acceleration configuration, formed by three metal disks with holes [see Fig. 5(a)]. In the first zone, the separation of promptly produced cations from molecules in high Rydberg states is achieved by applying a delayed (100 ns after the occurrence of the two laser pulses), negative voltage to the first disk and at the same time setting the second disk to ground potential [Fig. 5(b)]. This results in a weak electric field of 0.2–0.6 V/cm that decelerates the prompt ions. After a sufficient delay time of several microseconds the unaffected neutral molecules still excited to high Rydberg states have entered the second (repeller) zone (20 mm wide) where no field is present at that time. Then an electric field of 1000 V/cm is switched on, which field ionizes the high Rydberg molecules. The resulting threshold ions are accelerated and injected by the same electric field into a linear reflecting TOF mass spectrometer [Fig. 5(c)] [8]. After reflection, ions of different mass reach the multichannel

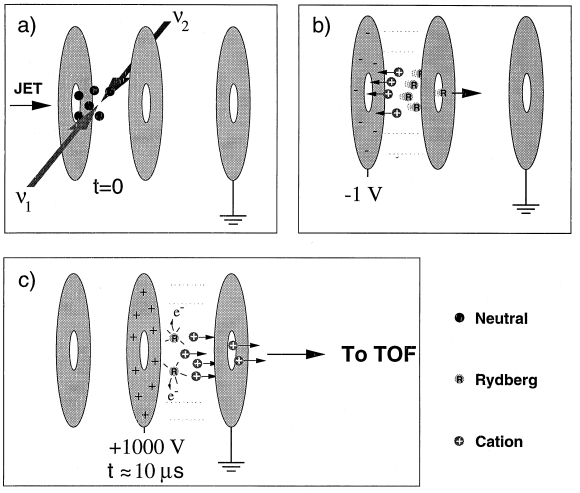

Fig. 5. Ion optics in a TOF for threshold ion detection. (a) Excitation of molecules within a molecular beam in a two-color two-photon process producing prompt ions and high Rydberg molecules. (b) Deceleration of the prompt ions in a weak electric separation field (0.2–0.6 V/vm). The Rydberg molecules are not affected by the field and pass the second electrode. (c) Ionization of the high Rydberg molecules in a strong field and acceleration of the so-produced threshold ions into the drift region of the TOF mass spectrometer.

plate detector at different times. The detector signal is recorded with gated "boxcar" integrators, then digitized and processed in a microcomputer system.

For obtaining intermediate state (REMPI) spectra no separation process is necessary. In this case the high positive voltage is applied to the first disk and the total ion current is recorded.

In this work, REMPI and threshold ion spectra of indole, indole · Ar, indole · H_2O, indole · benzene, phenol, phenol · H_2O, and 1-naphthol · H_2O were recorded.

4. Intermolecular bonds

Intermolecular cohesion forces and intramolecular chemical bonds both originate from electrostatic (coulombic) interactions. For the systems investigated in this work, one can distinguish different kinds of interaction contributing with different strengths to the various types of intermolecular bonds: (1) electrostatic forces between permanent multipoles, (2) induced multipole moments as a consequence of a charge redistribution when the constituents are approaching each other, (3) dispersion interaction originating from temporarily induced multipole moments due to fluctuating charge distributions, (4) exchange interaction, mainly responsible for repulsive forces when the distance of the binding partners is becoming smaller than the sum of the van der Waals radii, and (5) charge transfer resonance interaction playing a minor role for the complexes examined in this work.

The usual classification of the diverse types of intermolecular bonds is based on phenomenological characteristics like binding strength or chemical environment. Two important types of intermolecular bonds are the van der Waals (vdW) bond and the hydrogen bond (H-bond). The vdW interaction is long ranged and not restricted to a certain type of molecule or atom and is realized for noble gas atoms as well as large molecules. Its strength is mainly given by the polarizability and the permanent dipole moments of the constituents, and the typical BE varies between 0.5 and 200 meV. Values for the BEs of hydrogen bonds vary from 100 meV to 1 eV, which is nearly an order of magnitude larger than that of the vdW bonds. A hydrogen bond, X–H · · · Y, is active only at specific sites of the molecule, and thus directional and short-ranged, i.e. the interdistance between the proton H and Y is much shorter than the sum of the vdW radii. X is an electronegative atom (C, O, N, S, or halogen) and Y holds a free electron pair or a π orbital of an unsaturated multiple bond. The physical properties of the vdW and the H bond have been mainly studied in the bulk, e.g. with NMR or IR absorption spectroscopy, or high-pressure mass spectrometry (for an overview, see [1]). These experiments yielded averaged macroscopic parameters of the investigated systems, with many different unspecified bonds involved. It is desirable to get more detailed, microscopic information on the energetics and intermolecular potentials of defined intermolecular bonds at specific sites. Laser spectroscopic methods like REMPI or MATI applied to clusters produced in a cold supersonic jet expansion will be shown to yield valuable microscopic information.

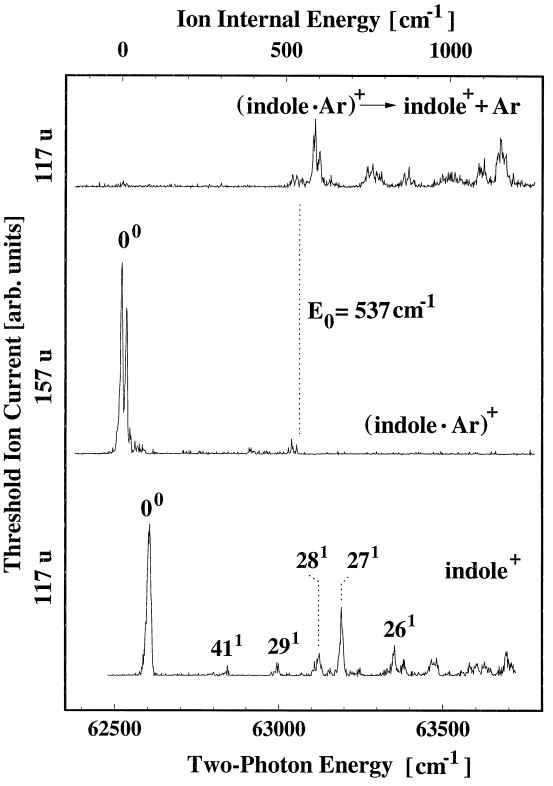

Fig. 6. Threshold ion spectra measured by a two-color two-photon excitation process with the first photon energy fixed to the vibrationless S_1 origin of the molecule or the cluster. (Bottom) bare indole, (middle) indole · Ar at the parent mass channel (157 u), (top) indole · Ar at the daughter mass channel (117 u). The broken line indicates the position of the field-free ionic dissociation threshold $E_0 = 537 \pm 10$ cm^{-1}.

4.1. van der Waals complexes

4.1.1. Indole · argon

Using the MATI technique described in Sec. 2.2, a threshold ion spectrum of bare indole (117 u) was recorded and is shown in the bottom trace of Fig. 6. It was measured in a resonance-enhanced two photon process with the frequency of the first laser fixed to the $S_1(^1L_b) \leftarrow S_0$, 0_0^0 transition at 35 232 cm^{-1}. The peaks indicate the individual ionization thresholds of various vibrational states of the indole cation (assignments, see [50]). The strongest peak of the indole threshold ion spectrum at a two-photon energy of 62 591 ± 5 cm^{-1} corresponds to the AIE of indole (0^0). It compares well with values from other groups (62 592 ± 4 cm^{-1} (ZEKE) [50], 62 598 ± 5 cm^{-1} (PIE) [51]).

A threshold ion spectrum of the indole · Ar vdW complex (157 u) is shown in the middle trace of Fig. 6. It was recorded with the frequency of the first laser fixed to the red-shifted (-26 cm^{-1}) $S_1(^1L_b) \leftarrow S_0$, 0_0^0 transition at 35 205 cm^{-1}. The origin of the vdW cluster (parent) threshold ion spectrum is located at 62 505 ± 5 cm^{-1} and shifted by 86 cm^{-1} to the red of the bare indole origin (62 591 ± 5 cm^{-1}). This means that the binding energy of the ionized cluster is larger by about 86 cm^{-1} than in its neutral ground state. The origin band of the cluster cation shows additional low frequency vibrational structure with four members of a progression with ≈14 cm^{-1} spacing. This arises from the excitation of a bending vdW mode and was also observed by Kimura and co-workers using ZEKE-PFI spectroscopy [50]. Similar signatures have been found for ionic complexes of Ar with other aromatic molecules [6,52–55].

We observe a breakdown of the signal in the parent ion spectrum for internal energies exceeding 537 cm^{-1} (dotted line) in a region with dense vibrational structure. The spectrum in the top panel of Fig. 6 represents the fragment (daughter) ion spectrum (117 u) of indole · Ar recorded simultaneously with the parent threshold ion spectrum (middle trace, 157 u) for the same excitation conditions. In the daughter channel signal appears for ion internal energies exceeding 487 cm^{-1}, which is about 50 cm^{-1} below the threshold for breakdown of the signal in the parent channel. As described above, the overlap region of ≈50 cm^{-1} with signal in the parent as well as in the daughter ion spectrum is caused by a coupling of high n members of Rydberg series converging to ionic states below the field-free dissociation threshold to lower n Rydberg levels converging to ionic states above the field-free dissociation threshold. In recent work we determined the field-free dissociation threshold by its extrapolation to zero field and found that it agrees with the breakdown threshold of the parent ion signal [56]. Thus, taking the breakdown of the parent ion signal as the field-free dissociation threshold, we obtain a dissociation threshold of $E_0 = 537 \pm 10$ cm^{-1} for the ionic indole · Ar complex. The dissoci-

ation threshold in the neutral ground state is calculated to $D_0 = E_0 - (IE_{indole} - IE_{indole \cdot Ar}) = 451$ cm^{-1}. This value is only slightly smaller than the theoretical value $D_0 = 480$ cm^{-1} obtained by Outhouse et al. and is within their experimental upper limit of 528 cm^{-1} [57].

4.1.2. Ar on aromatic microsurfaces

We compare the neutral ground state dissociation energy D_0 of indole · Ar of 480 cm^{-1} with binding energies of Ar attached to one-ring substrates like oxazole with $D_0 = 304$ cm^{-1} (ab initio) [58], benzene with $D_0 \leq 340$ cm^{-1} (experimental) [10] and $D_0 = 337$ cm^{-1} (ab initio) [58], fluorobenzene with $D_0 = 346 \pm 10$ cm^{-1} (experimental) [47] on the one hand, and three-ring substrates like carbazole with $D_0 = 530.4 \pm 1.5$ cm^{-1} (experimental) [59], dibenzo-*p*-dioxin with $D_0 = 527 \pm 18$ cm^{-1} (experimental) [12], and dibenzofuran with $D_0 \leq 521 \pm 12$ cm^{-1} (experimental) [12]) on the other hand. Most of the experimental values have been measured with the MATI technique as described above for the example of indole · Ar. All results are plotted in Fig. 7. These findings show that the binding energy of a single Ar atom to neutral aromatic molecules in the ground state is governed by the number of aromatic rings (delocalized π electrons) in the substrate for the same arrangement of the aromatic rings whereas the influence of heteroatoms in the substrate appears to be small. With increasing ring number the Ar binding energy increases and approaches the adsorption energy of Ar bound to the (001) surface of graphite which is ≈800 cm^{-1} [60]. Graphite has an infinite surface of hexagonal rings with delocalized π electrons. The value for the binding energy was found from a calculation representing an average value whereas the values in Fig. 7 measured with the MATI technique are microscopic values for a defined cluster species. Using higher temperatures in the nozzle, it seems to be possible to measure with the MATI technique the binding energies of even larger planar molecules with more aromatic rings, like coronene · Ar with seven aromatic rings. For this cluster, we expect a value of $D_0 \approx 720$ cm^{-1} from Fig. 7 and it is interesting to see whether this estimate can be confirmed by experiment.

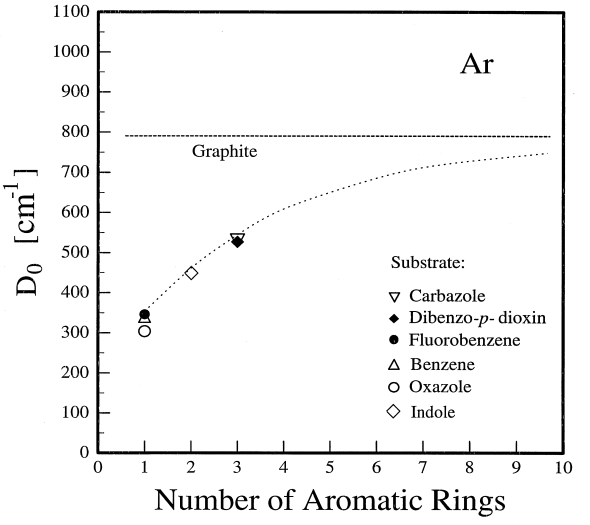

Fig. 7. Dissociation energies D_0 of neutral (planar aromatic molecule) · Ar complexes as a function of the number of aromatic rings. The dashed line indicates the adsorption energy of an Ar atom to the (001) surface of graphite. The dotted line connects the experimental results and gives an estimated extrapolation to larger microsurfaces.

4.2. Hydrogen bonding

4.2.1. Indole · H_2O and indole · C_6H_6

(a) Threshold ion spectra. The threshold ion spectrum of bare indole (117 u) of Fig. 6 is shown again on top of Fig. 8. For comparison, this spectrum and the lower two threshold ion spectra of the indole · H_2O and the indole · C_6H_6 cluster are displayed on a common ion internal energy scale though the absolute excitation energies differ for the three cases. The AIE of indole (AIE, 0^0) is 62 591 ± 5 cm^{-1}, as discussed in Sec. 4.1.1.

Indole · H_2O. The threshold ion spectrum of indole · H_2O obtained by way of the vibrationless intermediate state S_1, 0^0 of the cluster at 35 099 cm^{-1} [13,61] is shown in the middle trace of Fig. 8. We can identify intramolecular modes in the indole · H_2O spectrum by comparison with the indole MATI spectrum. Thus the

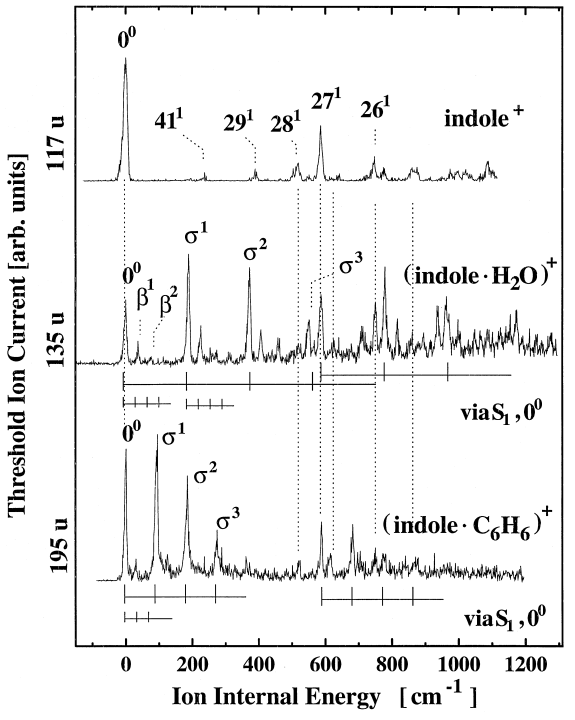

Fig. 8. Threshold ion spectra of indole (top), indole · H_2O (middle), and indole · C_6H_6 (bottom) on a common ion internal energy scale. The peaks in the indole$^+$ spectrum indicate the skeleton vibrations. In the cluster spectra, skeleton modes of indole are superimposed by intermolecular vibration progressions. The AIEs for indole, indole · H_2O, and indole · C_6H_6, indicated with 0^0, are 62 591 ± 5, 59 433 ± 5, and 59 833 ± 5 cm^{-1}, respectively.

AIE of the cluster is clearly given by the first peak in the threshold ion spectrum located at 59 433 ± 5 cm^{-1}. It is shifted by 3158 ± 5 cm^{-1} to the red of the bare indole origin, which is larger by a factor of 37 than the redshift of the AIE in the indole · Ar cluster. This means, there is a strong increase of the hydrogen bond energy after ionizing the cluster. We identify progressions of two different vibrational modes. We assign the strong progression with 189 cm^{-1} spacing (σ^1) to the intermolecular stretching mode which is supposed to form long progressions in the ionic spectra because the strongly increasing hydrogen binding strength after ionization shortens the hydrogen bond length and causes larger Franck-Condon factors for $\Delta\nu > 1$ transitions. The progression pattern is similar to that of the phenol · H_2O [62] and the 1-naphthol · H_2O (see the following). In addition, we observe a weak progression with 38 cm^{-1} spacing (β^1) starting at several vibrational bands. Most likely this is an intermolecular bending mode.

Indole · C_6H_6. In the bottom trace of Fig. 8, the threshold ion spectrum of indole · C_6H_6 is displayed. The AIE is found at 59 833 ± 5 cm^{-1} and thus shifted by 2785 ± 5 cm^{-1} to the red of the bare indole AIE, which is almost as large as in the case of indole · H_2O. The assignment of the AIE is corroborated by arguments similar to those discussed for the indole · H_2O complex. The threshold ion spectrum of indole · C_6H_6 is dominated by a 95 cm^{-1} vibration forming a long progression. This vibrational frequency is approximately half the frequency of (indole · H_2O)$^+$. This is what we expect for an intermolecular vibration with stretching character after comparison of the reduced masses μ of indole · H_2O and indole · C_6H_6 [$\sqrt{\mu_{\text{indole}\cdot C_6H_6}/\mu_{\text{indole}\cdot H_2O}} \approx 1.73$ in a diatomic molecule approximation and assuming the same binding strength for the N–H · · · π and the N–H · · · O hydrogen bond (see Sec. 5)].

(b) Dissociation energy. Next we recorded cluster and fragment threshold ion spectra of indole · H_2O and indole · C_6H_6 for higher ion internal energies. As an example, in Fig. 9 the cluster parent ion spectrum (bottom) and the daughter ion spectrum (top) of indole · H_2O are shown, recorded simultaneously in the range from zero up to 5000 cm^{-1} ion internal energy. In the low internal energy range up to 1500 cm^{-1}, the cluster ion spectrum shows long progressions of the σ mode discussed above (see Fig. 8). No signal is observed at the fragment mass in this low energy range and we conclude that no dissociation takes place. On the right-hand side of Fig. 9 two parent (lower set) and two daughter spectra (upper set) are displayed for an ion internal energy ranging from 4400 to 5250 cm^{-1}. They were obtained by pumping by way of the vibrationless S_1, 0^0 origin and the S_1, 26^1 intermediate state transition, respectively. Both parent ion spectra show a sudden breakdown of the signal while both daughter ion signals increase for the same ion internal energy threshold. Note, that the

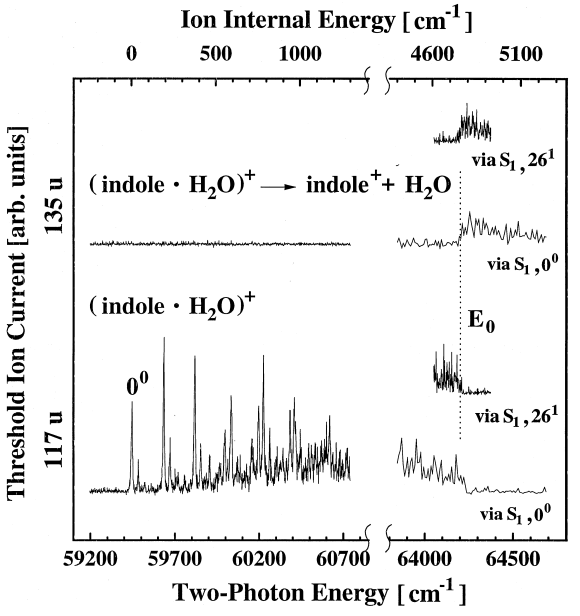

Fig. 9. (Left) Two threshold ion spectra of indole · H_2O at low (<1300 cm^{-1}) ion internal energy measured at the daughter mass, 117 u (top) and the parent mass, 135 u (bottom). Intermediate state of both two-photon excitation processes is the vibrationless origin ^1L_b, S_1. (Right) Two sets of threshold ion spectra of indole · H_2O at high ion internal energies measured at the daughter mass, 117 u (upper two spectra) and the parent mass, 135 u (lower two spectra). Each upper spectrum in both sets is obtained by means of the S_1, 26^1 intermediate state, lower spectra via pumping the vibrationless S_1 origin. The broken line indicates the field-free dissociation threshold E_0 = 4790 ± 10 cm^{-1}. Note that the measured value for E_0 is the same ion internal energy in both sets. (For explanation, see text.)

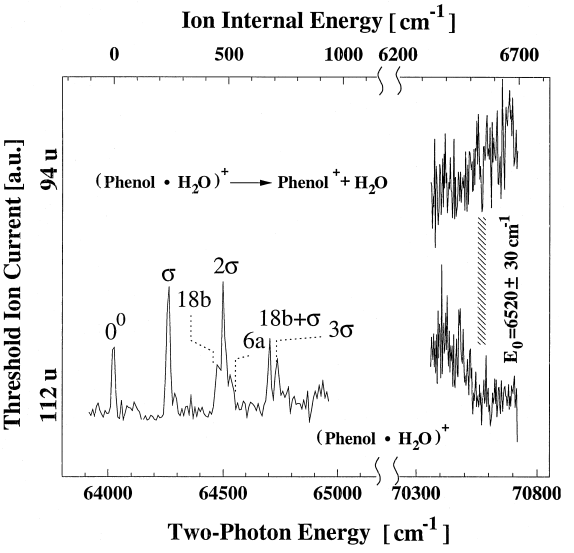

Fig. 10. (Left) Threshold ion spectrum of phenol · H_2O at low (<1200 cm^{-1}) ion internal energy measured at the parent mass, 112 u (bottom), by way of the vibrationless intermediate state origin S_1. (Right) Two threshold ion spectra of phenol · H_2O at high ion internal energies measured at the daughter mass, 94 u (upper spectrum) and the parent mass, 112 u (lower spectrum) by way of the vibrationless intermediate state origin S_1. The shaded rectangle indicates the dissociation threshold at an ion internal energy E_0 = 6520 ± 50 cm^{-1}.

same internal energy level has been reached by means of different intermediate states and excitation energies. This means that there is no mode selectivity of the dissociation energy and a statistical distribution of energy to all vibrational degrees of freedom occurs before dissociation. From the breakdown of the ion signal in the parent traces we find a field-free dissociation threshold of E_0 = 4790 ± 10 cm^{-1} for indole · water and the dissociation threshold in the neutral ground state is calculated to $D_0 = E_0 - (AIE_{indole} - AIE_{indole \cdot H_2O}) = 1632 \pm 15\ cm^{-1}$.

We performed similar measurements for the indole · C_6H_6 cluster [13]. They yield a dissociation energy of the ionic (indole · C_6H_6)$^+$ cluster of E_0 = 4581 ± 10 cm^{-1}, and of D_0 = 1823 ± 15 cm^{-1} in the neutral ground state. The increase of the binding energy after ionization is comparable to that of indole · H_2O, discussed previously. This and the absolute value of the binding energy supports our interpretation of a π-hydrogen bonding between the benzene π electrons and the aminohydrogen of indole, as will be discussed in more detail in Sec. 5.

4.2.2. Phenol · H_2O and 1-naphthol · H_2O

We would like to compare our results for the >N–H · · · O< hydrogen bond in indole · H_2O clusters with other types of hydrogen bonding. As further examples we measured threshold ion spectra of the phenol · H_2O and the 1-naphthol · H_2O cluster and investigated the –O–H · · · O< type hydrogen bonding. In addition, by choosing 1-naphthol one can study the influence of the additional aromatic ring on the hydrogen bonding in the neutral and the ionic cluster.

(a) Phenol · H_2O. On the left-hand side of Fig. 10 the parent threshold ion spectrum of phenol · H_2O (112 u)

is shown as recorded closely above the AIE. The excitation laser frequency was tuned to the vibrationless $S_1 \leftarrow S_0$ transition of phenol · H_2O at 35 996 ± 2 cm^{-1}. We measured an AIE of 64 024 ± 10 cm^{-1} for the cluster. The assignment of the vibrational peaks is adopted from [63,64]. An intermolecular mode at 240 cm^{-1} forming long progressions can be identified as a stretching σ vibration. Its frequency is larger by 25% than the value of 189 cm^{-1} found for the indole · H_2O cluster.

The result for the higher ion internal energy range from 6300 to 6700 cm^{-1} is shown on the right-hand side of Fig. 10. No vibrational structure can be resolved. In the lower trace, the parent threshold ion spectrum is displayed, whereas in the upper trace the daughter threshold ion spectrum is shown. The parent threshold ion current breaks down for an internal energy of E_0 = 6520 ± 50 cm^{-1}, while at the same time the daughter threshold ion current increases. In this case, finding the dissociation threshold turned out to be a nontrivial problem. The threshold ion signal is extremely weak because of the low Franck-Condon factors for transitions from the vibrationless S_1 state to the high-lying cationic vibrational states at ≈6500 cm^{-1}. For the spectrum shown in Fig. 10 the signal from several thousands laser pulses per frequency step had to be added. Because of the low signal to noise ratio, the cationic dissociation threshold E_0 can be determined only with moderate precision to E_0 = 6520 ± 50 cm^{-1} and the neutral binding energy D_0 is 1916 ± 30 cm^{-1}.

(b) 1-naphthol · H_2O. This cluster is particularly interesting. Comparing the binding energies and the cationic intermolecular stretching frequencies with the ones of the phenol · H_2O cluster one can check if there is an influence of the additional aromatic ring on the hydrogen bond. Moreover, 1-naphthol is of similar size as indole, making a comparison of the 1-naphthol · H_2O system to the indole · H_2O system reasonable. Therefore, we measured threshold ion spectra of 1-naphthol · H_2O pumped by way of different intermediate states. In the lower trace of Fig. 11, the threshold ion current spectrum obtained by means of the vibrationless S_1 state is shown. For

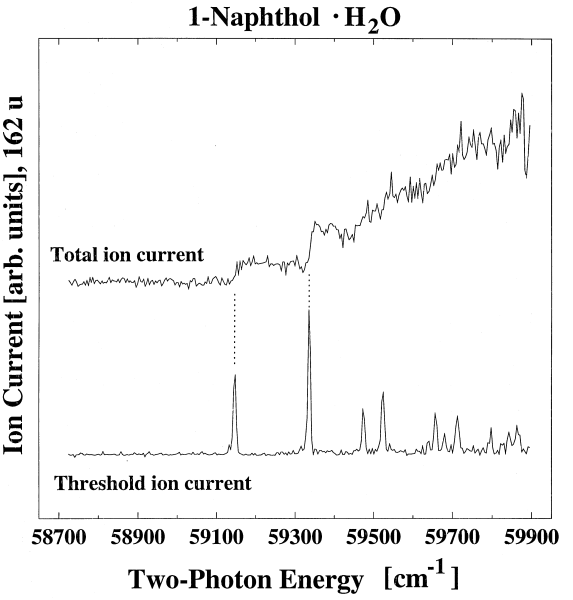

Fig. 11. (Lower trace) Threshold ion spectrum of 1-naphthol · H_2O at low ion internal energy measured by means of the vibrationless intermediate state S_1. (Upper trace) Total ion current spectrum with steps at the two lowest ionization thresholds coinciding with the peaks in the threshold ion spectrum.

demonstration the total ion current spectrum is displayed in the upper trace when measured via the same intermediate state. It shows steps at the individual cationic vibrational levels indicated by peaks in the threshold ion spectrum. As in phenol · H_2O and indole · H_2O, a long progression of an intermolecular vibrational stretching frequency of 190 cm^{-1} can be identified. This is 79% of the 240 cm^{-1} measured for the cationic phenol · H_2O cluster. The higher mass of the 1-naphthol cannot be the reason for this decrease, since the influence of the reduced masses on the stretching frequency would lead to a decrease of only 3% in a diatomic approximation. This indicates, that the hydrogen bond in the cationic 1-naphthol · H_2O cluster is weakened by the presence of the second ring.

Unfortunately, a direct determination of the ionic binding energy E_0 of the 1-naphthol · H_2O cluster in the threshold ion spectrum was not possible. When the energy of the ionizing photon (after excitation to the intermediate S_1 electronic state) is increased to be sufficient for the fragmentation of the cluster, mono-

Table 1
Intermolecular cationic stretching frequencies σ, cationic (E_0), and neutral (D_0) binding energies of hydrogen bonded clusters

	σ (cm^{-1})	E_0 (cm^{-1})	D_0 (cm^{-1})
Indole · H_2O	189	4790	1632
Indole · C_6H_6	95	4581	1823
Phenol · H_2O	240	6520	1916
1-Naphthol · H_2O	190	5547	2035

mer cations are produced in a one-color two-photon ionization process. They cannot be completely suppressed by the MATI separation process described in Sec. 3. As well as for phenol · water, the Franck-Condon factors are very small and because of a very weak threshold ion signal the ionic dissociation energy cannot be measured. However, using the value $D_0 = 2035 \pm 69$ cm^{-1} of the neutral 1-naphthol · H_2O cluster recently measured with a special depletion technique by Bürgi et al. [65] we can calculate the ionic binding energy of 1-naphthol · H_2O to $E_0 = 5547 \pm 15$ cm^{-1}. This is possible because an accurate value for the AIE is available from our MATI experiments (see Fig. 11). The binding energy of (1-naphthol · H_2O)$^+$ is lower by 15% than the value of $E_0 = 6520$ cm^{-1} of (phenol · H_2O)$^+$. This is in line with the smaller frequency of the intermolecular stretching vibration in the cationic 1-naphthol · H_2O cluster, as discussed previously. Interestingly, the situation is reversed for the neutral species, where the binding energy of 1-naphthol · H_2O is slightly higher, as discussed below in detail.

5. Discussion

In Table 1, all experimental results for the vibrational frequencies and the binding energies are summarized and are to be discussed in this section.

5.1. >N–H · · · π hydrogen bond

For the indole · C_6H_6 cluster, we measured a binding energy of $E_0 = 4581 \pm 10$ cm^{-1} and $D_0 = 1823 \pm 15$ cm^{-1} in the ionic and neutral cluster, respectively. The values are much larger than the

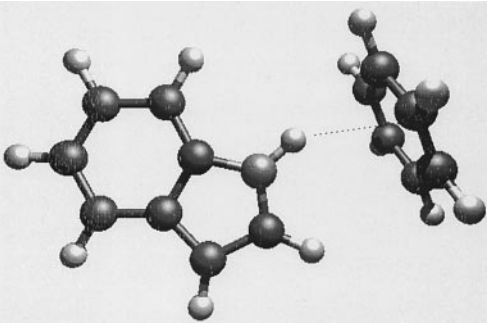

Fig. 12. Artist's view of the proposed S_0 structure of the indole · C_6H_6 cluster with a N–H · · · π-type hydrogen bond. This structure is supported by spectroscopic results, energetic considerations and medium-level ab initio calculations. For explanation, see text.

binding energies of van der Waals bound mixed and homogeneous dimeric complexes of aromatic molecules with many atom–atom dispersion interactions, like benzene, *p*-difluorobenzene, and toluene. For these dimers experimental [8,21,66–69] and in part theoretical values [67,70,71] have been obtained. For the extensively studied neutral benzene dimer ab initio calculations yielded for the parallel-displaced and the T-shaped structure nearly the same stabilization energy of about 2.3 kcal/mol (800 cm^{-1}) [72]. Breakdown measurements yielded 566 ± 80 cm^{-1} for the benzene homo dimer and 645 ± 120 cm^{-1} for the *p*-difluorobenzene · benzene and the toluene · benzene heterodimers [21]. Even if one takes into account that indole is larger than the molecular components of the clusters mentioned above the factor of 2 larger binding energy of the indole · C_6H_6 cluster cannot be explained by the resulting larger van der Waals interaction. This, and the long progressions of an intermolecular stretching vibration in the threshold ion spectrum of the indole · C_6H_6 cluster similar to that of the indole · H_2O cluster (see Fig. 8) indicate that the interaction is dominated by hydrogen bonding involving the >N–H group of indole and the benzene π cloud serving as an electron donor as illustrated in Fig. 12. This is corroborated by the strong increase of the binding strength in indole · C_6H_6 after ionization which was found to be typical for hydrogen bonds. Our finding is supported by ab initio structure optimization calculations at the Hartree-Fock level (UHF/

3-21G*). Of course, calculations at this level have to be taken with care for such a large system, but the theoretical result does not contradict the experimental found structure. Both, experimental and theoretical result support our conclusion of a π hydrogen bonding.

5.2. –O–H · · · O< hydrogen bond

We found an increase of the hydrogen bond strength in all presented hydrogen bonded clusters after ionization by a factor ranging from 2.5 to 4. As shown in Sec. 4.2.2, the frequency of the intermolecular stretching vibration as well as the binding energy E_0 of the (1-naphthol · H_2O)$^+$ cation are noticeably smaller than in case of the (phenol · H_2O)$^+$. This means that the H bond in the cluster cation is weakened by the presence of the additional aromatic ring. On the other hand, the binding energy D_0 of the neutral 1-naphthol · H_2O cluster is larger than D_0 of phenol · H_2O.

To explain these results, we investigated the consequences of the electron loss after ionization on the electron distribution (ED) within the molecule as well as the effect of the water attachment, for 1-naphthol. For this we calculated electron distributions (ab initio) using the GAUSSIAN 98 package. After geometry optimization of the monomer and the cluster cation at medium level (correlation consistent double-zeta basis set [cc-pVDZ] augmented by diffuse functions of the 6-31+G basis set at the heavy atoms), we used the so obtained nuclear positions as an input for calculations of the EDs of the cations as well as the neutral systems at the higher MP2/6-311++G** level. The net electron displacements after ionization were obtained after subtracting the EDs of the cations from the EDs of the neutrals. Similarly, we obtained a map of the charge displacement upon clustering after subtracting the EDs of the water and the 1-naphthol monomer from the ED of the cluster.

In Fig. 13(a), calculated changes of the ED of 1-naphthol in the molecular plane caused by ionization are visualized as a contour plot. Negative density values (electron loss) are represented by black lines, whereas positive values (electron gain) are light gray.

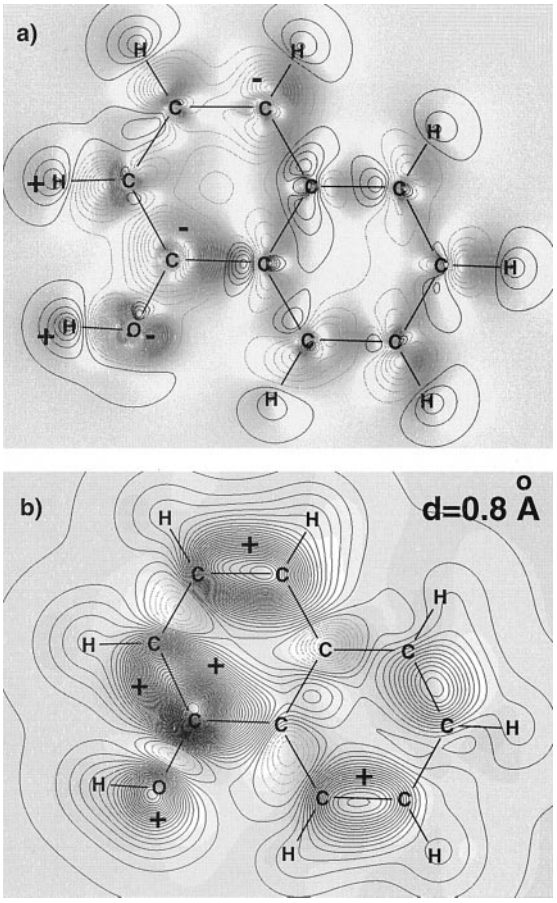

Fig. 13. Contour plot of the difference of ED in the 1-naphthol cation from that of the neutral molecule, calculated with ab initio methods. (a) Molecular plane. Note, that the ED increases at the positions of the C and O atoms though the total charge is positive. (b) Plane parallel displaced by 0.8 Å. ED decreases at all atoms.

Note, that the ED after ionization even increases close to the C and O atoms and decreases at the H atoms, particularly at the O–H hydrogen. Regions of large electron loss are marked by plus sign (because they are positively charged), whereas regions of large electron gain are marked by minus sign in Fig. 13. The situation changes for the electron density in a plane displaced by 0.8 Å parallel above or below the aromatic rings. There, a strong overall decrease of electron density is found [see Fig. 13(b)]. From this the following is clear. (1) The water molecule with a permanent dipole moment of 1.85 debye is attracted by the overall positively charged naphthol molecule.

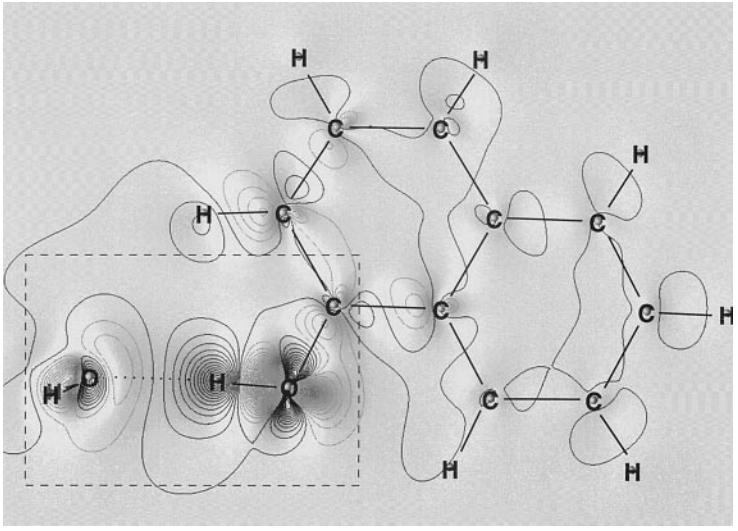

Fig. 14. Contour plot of the difference of electron density in the 1-naphthol · H_2O cluster from that of the unclustered molecules, calculated with ab initio methods. (a) Electron density mainly changes at the OH group, the H_2O, and also at the C and O atom in the two position of the 1-naphthol. The dashed line indicates the quasilinear hydrogen bond O–H · · · O–H.

A simple calculation, assuming the positive charge being concentrated in the center of the 1-naphthol shows that this would lead to an increase of the binding energy of ≈1500 cm^{-1}. (2) After ionization, the ED increases at the O atom and decreases at the hydroxyl H atom, causing a stronger polarization and a further strengthening of the hydrogen bond compared to the neutral cluster. This is in good agreement with our experimental finding. The stronger cationic H bond for the smaller phenol in the phenol · H_2O cluster can be explained as follows. After ionization, the electron density decreases uniformly in the aromatic ring system. For a smaller aromatic molecule, the distance of the water (which is held at a fixed position) to the center of charge is smaller and the water dipole is more strongly attracted, as indeed observed for the phenol · H_2O cluster.

In the neutral ground state, the situation is different. Here the binding energy of the phenol · H_2O is smaller by 6% than that of 1-naphthol · H_2O. It appears that the additional aromatic ring increases the bond strength in the neutral cluster. This can be attributed to an additional weak van der Waals (dispersion) interaction induced by the additional π electrons and neighbored H atoms. It is more important in the neutral cluster since strong charge-induced contributions are absent in this case.

In Fig. 14, the change of the ED in the neutral naphthol molecule caused by the hydrogen bond is displayed. In Fig. 14, only induced but no permanent dipole moments are visible which contribute most to the H bond. There is an attractive force between the positively charged H atom of the O–H group and the two negatively charged free electron pairs at the O atom of the H_2O molecule. In Fig. 14(a), not only the charge shifts directly at atoms involved in the H bond can be identified, but also charge shifts at the H atom in the two position and in the aromatic ring. This means that an additional, van der Waals type interaction between the water and the 1-naphthol is present and contributes substantially to the intermolecular bonding.

5.3. >N–H · · · O< hydrogen bond

Comparing the experimental results for the binding energies of indole · H_2O to 1-naphthol · H_2O, we find an increase of 15% for E_0 and 24% for D_0 of the latter. This is in line with the general rule that an >N–H · · · O< type hydrogen bond is weaker than an

–O–H · · · O< type hydrogen bond, because of the higher electron affinity of oxygen compared to that of nitrogen. Here we presented accurate values for a selected specific hydrogen bond that can be compared with theoretical calculations. Further, it would be highly interesting to compare the binding energies of indole · H_2O to binding energies of clusters with larger heterocyclic solutes, e.g. carbazole. In this way one could study the influences of additional aromatic rings on a >N–H · · · O< type hydrogen bond.

6. Summary and conclusion

In this work we demonstrated that, combining optical excitation with mass spectrometric detection, yields fundamental insight into the nature of weak intermolecular bonds of organic molecules. An important precondition is the production of ions excited to selected states or at defined internal energies. This is possible with the technique of mass analyzed threshold ionization. We applied this technique to the investigation of small isolated clusters produced in a supersonic cold molecular beam. We studied a series of clusters of prototype aromatic molecules with noble gas, water and a second aromatic molecule, where different kinds of intermolecular bondings exist. We were able to investigate the intermolecular bonding in neutral as well as in ionized clusters and thus work out the changes produced by the different charge distributions. As a result accurate values for microscopic binding energies of different types of hydrogen bonds in indole · H_2O, indole · C_6H_6, phenol · H_2O, and 1-naphthol · H_2O in their neutral and cationic ground states were found. Generally, the intermolecular binding energy of all investigated hydrogen bonded clusters is larger by a factor of 2.5–4 than in neutral clusters. The dependence of the binding energy on the solute molecule size was investigated for the clusters phenol · H_2O and 1-naphthol · H_2O. The ionic binding energy (E_0) is found to decrease with increasing aromatic solutes, whereas for the neutral species the situation is reversed. We found evidence for a structure of indole · C_6H_6 with a linear N–H · · · π type hydrogen bond. The hydrogen bonding character is concluded from the large dissociation energies E_0 and D_0, the strongly increasing binding energy after ionization, the sharp vibrational structure, and the vibrational energies in the threshold ion spectrum. Comparing the N–H · · · O with an O–H · · · O type hydrogen bond, the binding energy turned out to be higher in the O–H · · · O type hydrogen bond.

Detailed experimental information on the energetics and intermolecular dynamics of the van der Waals and in particular of the hydrogen bond is important for the understanding of their role in the formation of the tertiary (three-dimensional) structure of proteins and peptides. In particular the hydrogen bond between organic molecules like indole and benzene has prototype character for the understanding of complex biological systems and yields basic information for an explanation of the structure and functionality of biomolecules. Future investigations should be extended to derivatives of the presented molecules with larger aromatic chromophores. Further, bicromophoric clusters, similar to indole · C_6H_6, are suitable prototype systems for investigation of charge transfer processes which are fundamental primary processes in biochemistry.

Acknowledgements

The authors wish to thank Thomas Grebner and Klaus Siglow for valuable discussions. Financial support from the Deutsche Forschungsgemeinschaft and the Fonds der Chemischen Industrie is gratefully acknowledged.

References

[1] P.L. Huyskens, W.A.P. Luck, T. Zeegers-Huyskens, Intermolecular Forces, Springer, Berlin, 1991.
[2] D.H. Levy, Science 214 (1981) 263.
[3] B. Brehm, E. von Puttkamer, Z. Naturforsch. 22a (1967) 8.
[4] T. Baer, in Gas Phase Ion Chemistry, M.T. Bowers (Ed.), Academic, New York, 1979, p. 153.
[5] L. Zhu, P.M. Johnson, J. Chem. Phys. 94 (1991) 5769.
[6] H. Krause, H.J. Neusser, J. Chem. Phys. 97 (1992) 5923.

[7] Th.L. Grebner, H.J. Neusser, Int. J. Mass Spectrom. Ion Processes 185/186/187 (1999) 532.
[8] B. Ernstberger, H. Krause, A. Kiermeier, H.J. Neusser, J. Chem. Phys. 92 (1990) 5285.
[9] H.J. Neusser, H. Krause, Chem. Rev. 94 (1994) 1829.
[10] H. Krause, H.J. Neusser, J. Chem. Phys. 99 (1993) 6278.
[11] Th.L. Grebner, H.J. Neusser, Chem. Phys. Lett. 245 (1995) 578.
[12] Th.L. Grebner, R. Stumpf, H.J. Neusser, Int. J. Mass Spectrom. Ion Processes 167/168 (1997) 649.
[13] J.E. Braun, Th.L. Grebner, H.J. Neusser, J. Phys. Chem. 102 (1998) 3273.
[14] X. Zhang, J.D. Pitts, R. Nadarajah, J.L. Knee, J. Chem. Phys. 107 (1997) 8239.
[15] G. Lembach, B. Brutschy, J. Chem. Phys. 107 (1997) 6156.
[16] G. Lembach, B. Brutschy, Chem. Phys. Lett. 273 (1997) 421.
[17] M. Gerhards, C. Unterberg, S. Schumm, J. Chem. Phys. 111 (1999) 7966.
[18] S.R. Haines, C.E.H. Dessent, K. Müller-Dethlefs, J. Chem. Phys. 111 (1999) 1947.
[19] N. Ohmichi, Y. Malinovich, J.P. Ziesel, C. Lifshitz, J. Phys. Chem. 93 (1989) 2491.
[20] H.J. Neusser, H. Krause, Int. J. Mass Spectrom. Ion Processes 131 (1994) 211.
[21] B. Ernstberger, H. Krause, H.J. Neusser, Z. Phys. D 20 (1991) 189.
[22] H. Krause, B. Ernstberger, H.J. Neusser, Chem. Phys. Lett. 184 (1991) 411.
[23] Th.F. Gallagher, Rydberg Atoms, Cambridge Monographs, Cambridge, 1994.
[24] C. Fabre, S. Haroche, Spectroscopy of One- and Two-Electron Rydberg Atoms, R.F. Stebbings, F.B. Dunning, Cambridge University Press, Cambridge, 1983.
[25] C. Bordas, P.F. Brevet, M. Broyer, J. Chevaleyre, P. Labastie, J.P. Petto, Phys. Rev. Lett. 60 (1988) 917.
[26] D. Bahatt, U. Even, R.D. Levine, J. Chem. Phys. 98 (1993) 1744.
[27] R.G. Neuhauser, K. Siglow, H.J. Neusser, J. Chem. Phys. 106 (1997) 896.
[28] K. Siglow, H.J. Neusser, Faraday Discuss. 115 (2000) 245.
[29] M. Bixon, J. Jortner, J. Phys. Chem. 99 (1995) 7466.
[30] W.A. Chupka, J. Chem. Phys. 98 (1993) 4520.
[31] W.A. Chupka, J. Chem. Phys. 99 (1993) 5800.
[32] F. Merkt, R.N. Zare, J. Chem. Phys. 101 (1994) 3495.
[33] J. Jortner, M. Bixon, J. Chem. Phys. 102 (1995) 5636.
[34] M.J.J. Vrakking, D.M. Villeneuve, A. Stolow, J. Chem. Phys. 102 (1995) 8818; 102 (1995) 8833.
[35] S.G. Grubb, C.E. Otis, R.L. Whetten, E.R. Grant, A.C. Albrecht, J. Chem. Phys. 82 (1985) 1135.
[36] R.L. Whetten, S.G. Grubb, C.E. Otis, A.C. Albrecht, E.R. Grant, J. Chem. Phys. 82 (1985) 1115.
[37] K. Müller-Dethlefs, M. Sander, E.W. Schlag, Chem. Phys. Lett. 112 (1984) 291.
[38] F. Merkt, R.J. Rednall, S.R. Mackenzie, T.P. Softley, Phys. Rev. Lett. 76 (1996) 3526.
[39] K. Müller-Dethlefs, O. Dopfer, T.G. Wright, Chem. Rev. 94 (1994) 1845.
[40] K. Müller-Dethlefs, E.W. Schlag, E.R. Grant, H. Wang, B.V. McKoy, Adv. Chem. Phys. 90 (1995) 1.
[41] K. Müller-Dethlefs, J. Electron Spectrosc. Relat. Phenom. 75 (1995) 35.
[42] K. Siglow, H.J. Neusser, J. Chem. Phys. 112 (2000) 647.
[43] P.R. Kemper, P. Weis, M.T. Bowers, Int. J. Mass Spectrom. Ion Processes 160 (1997) 17.
[44] S.S. Hunnicutt, T.M. Branch, J.B. Everhart, D.S. Dudis, J. Phys. Chem. 100 (1996) 2083.
[45] L. Oudejans, R.E. Miller, J. Phys. Chem. A 101 (1997) 7582.
[46] H. Krause, H.J. Neusser, J. Photochem. Photobiol. A 80 (1994) 73.
[47] Th.L. Grebner, P. von Unold, H.J. Neusser, J. Phys. Chem. A 101 (1997) 158.
[48] R. Neuhauser, K. Siglow, H.J. Neusser, Phys. Rev. Lett. 80 (1998) 5089.
[49] K. Siglow, R. Neuhauser, H.J. Neusser, J. Chem. Phys. 110 (1999) 5589.
[50] T. Vondrak, S. Sato, K. Kimura, J. Phys. Chem. A 101 (1997) 2384.
[51] J. Hager, M. Ivanco, M.A. Smith, S.C. Wallace, Chem. Phys. 105 (1986) 397.
[52] X. Zhang, J.M. Smith, J.L. Knee, J. Chem. Phys. 97 (1992) 2843.
[53] M. Takahashi, H. Ozeki, K. Kimura, J. Chem. Phys. 96 (1992) 6399.
[54] M.C.R. Cockett, K. Okuyama, K. Kimura, J. Chem. Phys. 97 (1992) 4679.
[55] Th.L. Grebner, H.J. Neusser, Int. J. Mass Spectrom. Ion Processes 159 (1996) 137.
[56] Th.L. Grebner, P. von Unold, H.J. Neusser, J. Phys. Chem. A 101 (1997) 158.
[57] E.A. Outhouse, G.A. Bickel, D.R. Demmer, S.C. Wallace, J. Chem. Phys. 95 (1991) 6261.
[58] E. Kraka, D. Cremer, U. Spoerel, I. Merke, W. Stahl, H. Dreizler, J. Phys. Chem. 99 (1995) 12466.
[59] T. Droz, T. Bürgi, S. Leutwyler, J. Chem. Phys. 103 (1995) 4035.
[60] W.A. Steele, Surf. Sci. 36 (1973) 317.
[61] M.J. Tubergen, D.H. Levy, J. Phys. Chem. 95 (1991) 2175.
[62] O. Dopfer, G. Reiser, K. Müller-Dethlefs, E.W. Schlag, S.D. Colson, J. Chem. Phys. 101 (1994) 974.
[63] O. Dopfer, G. Reiser, R. Lindner, K. Müller-Dethlefs, Ber. Bunsenges. Phys. Chem. 96 (1992) 1259.
[64] P. Hobza, R. Burci, V. Spirko, O. Dopfer, K. Müller-Dethlefs, E.W. Schlag, J. Chem. Phys. 101 (1994) 990.
[65] T. Bürgi, T. Droz, S. Leutwyler, Chem. Phys. Lett. 246 (1995) 291.
[66] I. Nishiyama, I. Hanazaki, Chem. Phys. Lett. 117 (1985) 99.
[67] A. de Meijere, F. Huisken, J. Chem. Phys. 92 (1990) 5826.
[68] M. Meot-Ner, P. Hamlet, E.P. Hunter, F.H. Field, J. Am. Chem. Soc. 100 (1978) 5466.
[69] A. Kiermeier, B. Ernstberger, H.J. Neusser, E.W. Schlag, J. Phys. Chem. 92 (1988) 3785.
[70] P. Hobza, H.L. Selzle, E.W. Schlag, J. Chem. Phys. 93 (1990) 5893.
[71] B.W. van de Waal, Chem. Phys. Lett. 123 (1986) 69.
[72] P. Hobza, H.L. Selzle, E.W. Schlag, J. Phys. Chem. 100 (1996) 18790.